APPLICATION OF THE METHOD OF EFFECTIVE SUSCEPTIBILITY TO THE SIMULATION OF SCANNING NEAR-FIELD OPTICAL MICROSCOPY

V.O. VASILENKO[1], V.Z. LOZOVSKI[1,2]

UDC 535
©2009

[1]**Taras Shevchenko Kyiv National University**
(5 Build., 2, Academician Glushkov Ave., Kyiv 03022, Ukraine; e-mail: verion@univ.kiev.ua),

[2]**V. Lashkarev Institute of Semiconductor Physics, Nat. Acad. of Sci. of Ukraine**
(45, Nauky Prosp., Kyiv 03028, Ukraine)

We consider the peculiarities of the formation of near-field patterns in ordinary scanning near-field optical microscopy (SNOM) and in ultrafast SNOM (UF-SNOM). The method of effective susceptibility for calculations of near-field images is discussed. The method is based on an analytic solution of the Lippmann–Schwinger equation. By the examples of objects with simple form such as a parallelepiped and a triangular pyramid, we demonstrate the results of numerical calculations of near-field images. It is shown that the form of a near-field image depends on the mutual orientation of the polarization vectors of the probing field of a microscope and the field registered by a detector. We present the results of numerical calculations of near-field images which are obtained in ultrafast SNOM on the study of an exciton cloud generated by a laser pulse. The numerical analysis of the spatial configurational resonances of an exciton cloud which is relaxing. It is shown that, in this case, the nonlinear interactions in the system should be taken into account. and *etc.*

1. Introduction

In recent years, the studies of nano-sized systems are significantly intensified with the purpose to produce new artificial materials for microelectronics, optoelectronics, and photonics. The new technologies allow one to fabricate systems with controlled morphology such as quantum dots, molecular complexes on surfaces, and photonic crystals [1–3]. The systems obtained due to these new technologies require to develop the methods of studies allowing one to obtain the information about a system without its fracture such as non-destructive methods of high-resolution scanning microscopy, including scanning tunneling microscopy [4], scanning atomic force microscopy [5], scanning near-field microscopy [6]. In addition to the information about the morphological specific features of micro- and nanosystems, there frequently arises the necessity to know the distribution of a local field. Such a task is posed, for example, in the investigation of the propagation of surface waves in two-dimensional

photonic-crystalline structures [7]. The most adequate methods to solve this problem are those of SNOM [8].

The studies of nanoobjects with the help of ordinary methods of optical microscopy are faced with serious limitations which have the basic character. There exists the physical limit, the minimum distance between two points, for which these points cannot be distinguished. Such a distance is called the diffractive limit of the resolution and is defined by the formula [9]

$$d = \alpha \frac{\lambda}{2n\sin\theta}, \tag{1}$$

where the coefficient α is determined by the geometry of the experiment, λ – light wavelength, n – refractive index of the environment, and θ — angle, at which the objective is seen from a given point of the system under study. It is seen from formula (1) that the diffractive limit of the resolution can be decreased by decreasing the light wavelength and by increasing the refractive index. But even if we will use ultraviolet sources and the newest technologies in the fabrication of objectives, the minimum distance d remains on a level of 200 nm within the scope of ordinary optical microscopy. This limitation can be overcome only if the mechanism of the formation of images will be basically changed. For example, the use of electrons instead of photons decreases essentially the diffractive limit, since the electron wavelength is less than the photon wavelength. But the operation of such a microscope requires high vacuum. This condition is not always eligible.

On the other hand, the contemporary studies require frequently to visualize the distribution of fields in nanosystems. The statement of such a task should also need to possess the adequate physical approaches and, as a result, the relevant facilities. These circumstances forced researchers to return to the old idea of the construction of a subwave microscope. The main

reasoning concerning the construction of an optical microscope with high resolution was first advanced by Synge as early as in 1928 [10]. The technology of that time did not allow one to realize the Synge's ideas in an operating device. The main Synge's idea was the illumination of an object through a hole with size which should be significantly less than the light wavelength. In this case, the distance between the object and the hole must be less than a half of the wavelength used in a device. Thus, by illuminating the object, light has no time to diffract at such small distances. As a result the resolution of a device depends only on the hole size and is independent of the wavelength of a probing light. On the formation of an image, the hole (probe) moves along the object surface, and the optical response of the system is synchronously recorded. The Synge's work was forgotten till 1982, when a resolution of $\lambda/60$ was experimentally attained with the use of microwaves with a wavelength of about 3 cm [11]. In 1984, the first optical near-field microscope, in which the resolution reached $\lambda/20$, was constructed [12]. This success stimulated the subsequent development of various configurations of SNOM [13]).

2. Main Principles of SNOM

We will formulate now the basic physical principles of SNOM. To this end, let us consider the formation of the image of a corrugated surface (see Fig. 1) by the ideal optical system. As was mentioned above, the resolution of the ideal optical device meets the fundamental limitations which are related to the wave nature of light. Namely, the resolution, i.e. the ability to distinguish the optical signals from two adjacent points of an object (for definiteness, let them be two adjacent humps of a corrugated surface), is bounded by relation (1) at a fixed wavelength of the testing emission. What will happen while the grating period is decreasing? To answer this question, we write the field on a detector ($z > 0$) in the so-called $\vec{k}, z$ representation

$$\vec{E}(\vec{k}, z) = \vec{e}(\vec{k})e^{i\eta z}, \qquad (2)$$

where $\eta = \sqrt{k_0^2 - k^2}$ ($k_0 = \omega/c$, $\mathrm{Re}\,\eta > 0$, $\mathrm{Im}\,\eta > 0$). By passing into the direct space, we have

$$\vec{E}(\vec{R}) = \int \frac{d\vec{k}}{(2\pi)^2} \vec{e}(\vec{k})\, e^{i\eta z + i\vec{k}\vec{r}}. \qquad (3)$$

It is seen that if the characteristic wave vectors of the field are such that $|\vec{k}| \le k_0$, the propagation constant η is real, and field (3) is radiative. That is, it can be fixed by a detector at a certain distance z_0 from the grating.
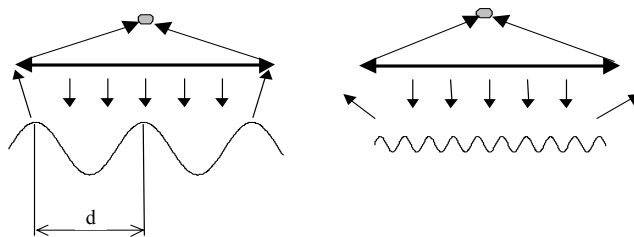
Fig. 1. Formation of the image of a corrugated surface

The less the grating period, the greater the part of the scattered light characterized by the wave vectors $|\vec{k}| \ge k_0$ corresponding to the fields

$$\vec{E}_{ev}(\vec{r}, z_0) = \int \frac{d\vec{k}}{(2\pi)^2} \vec{e}(\vec{k})e^{i\vec{k}\vec{r}}e^{-\mathrm{Im}\eta \cdot z_0}, \qquad (4)$$

which rapidly decrease, as the distance to the grating increases. Such fields have a special name – *evanescent fields*. It is clear that just they contain the information about small-scale inhomogeneities of a scatterer. Thus, the field passes in the evanescent region with decrease in the grating period. When the condition that the wave vectors characterizing the field should be less than k_o becomes satisfied, all the field scattered by inhomogeneities (i.e. it contains the information about the structure of inhomogeneities) becomes evanescent. That is, in order to obtain the the information about the inhomogeneities with characteristic sizes significantly less than the wavelength of the probing field, we must learn to register evanescent waves. Since the evanescent fields transfer no energy, this means that it is necessary to create the conditions for the transfer of an evanescent wave into the radiation region. To satisfy this condition, we can, for example, introduce an additional inhomogeneity in the system, because it causes a local breaking of the momentum conservation law, and a part of the field energy can be emitted. We note that we considered, all the time, the interaction of a particle or inhomogeneities of the object which have linear sizes much less than the wavelength of a probing field. In this case, the main purpose is to study the field distribution in the direct vicinity of an inhomogeneity and on characteristic length scales of the order of the size of a particle. This is a full analog of the radiophysical problem of a near zone on the propagation of waves. By analogy, the problem was named "*near-field optics*".

To register small-scale inhomogeneities of a system (e.g., quantum points or molecular complexes on the semiconductor surface), it is necessary to construct such devices which would allow one to register evanescent
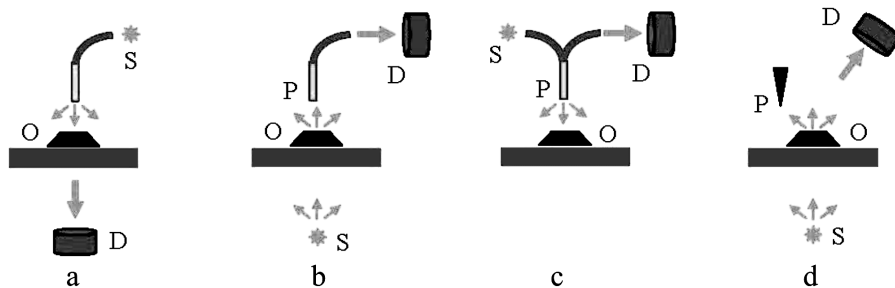
Fig. 2. Three types of scanning near-field microscopes: a – probe-lighter, b – probe-collector, c – probe which is simultaneously a lighter and a collector, d – apertureless probe. Designations: S – probing emission source, D – detector, P – probe tip, O – object under study
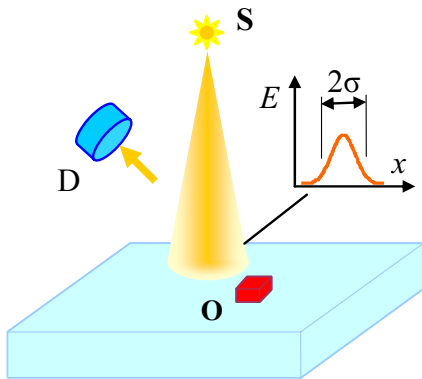
Fig. 3. Scheme of scanning optical microscopy with a Gauss beam: S – probing emission source, O – object under study; σ – effective radius of the illuminated spot

fields. According to this idea, four configurations of near-field microscopes with the transfer of a part of evanescent fields into the radiation region can be proposed (Fig. 2). The general feature of the construction of such microscopes is the positioning system which allows one to scan with a probe in a plane at a small distance to the object under study. In this case, the probe can be positioned with a high resolution in the scanning plane (the mechanism of this system is completely analogous to that of scanning systems in tunneling or atomic force microscopy).

The idea of the first type of a SNOM-microscope consists in that a probe with sizes less than characteristic wavelengths of the emission in use is positioned at nanodistances from the object (Fig. 2,a). The intensity of the field scattered by the probe will be, obviously, proportional to the intensity of the evanescent field at the point, where the probe is located. By moving the probe along the object surface and by synchronously recording a response of the system with the help of an ordinary optical detector which is placed in the far zone, one can obtain the information about the object.

Another, more widely used approach consists in the use of a probe simultaneously as an illumination source and as a receiver of the reemitted light (Fig. 2,b). In this case, if the probe tip in in the near zone, then it scatters evanescent waves, and a wave, whose characteristics depend on a local field at the point where the probe is located, propagates along the probe toward a detector. A version of the previous type of SNOM is the approach where both the illumination of an object and the gathering of a local field with the subsequent transfer of a signal to a detector occur via the probe (Fig. 2,c).

One more method of transformation of an evanescent wave into a radiation-propagating mode can be proposed. Namely, the illumination source can be placed in the far zone where a detector is located as well. In the near zone near an object, a passive probe is moving, and the probe tip is placed at a distance from the object which is significantly less than the wavelength of the illuminating field (Fig. 2,d). Since the probe is the reason for the local breaking of the momentum conservation law, it can reemit a part of the evanescent field in the radiation mode. Just this field is registered by a detector.

It is worth noting that, due to the development of optofiber technologies, a growing attention is recently paid to the studies in the scope of scanning optical microscopy, where the role of a probe is played by strongly focused beams whose shape is close to the Gauss one. Such studies have particular meaning for the determination of nonlinear optical characteristics of mesoobjects. A scheme of measurements by the method of scanning optical microscopy (SOM) is presented in Fig. 3.

However, the above-considered types of microscopy are unsuitable for fast dynamical processes such as the transport, scattering, and relaxation of free carriers or
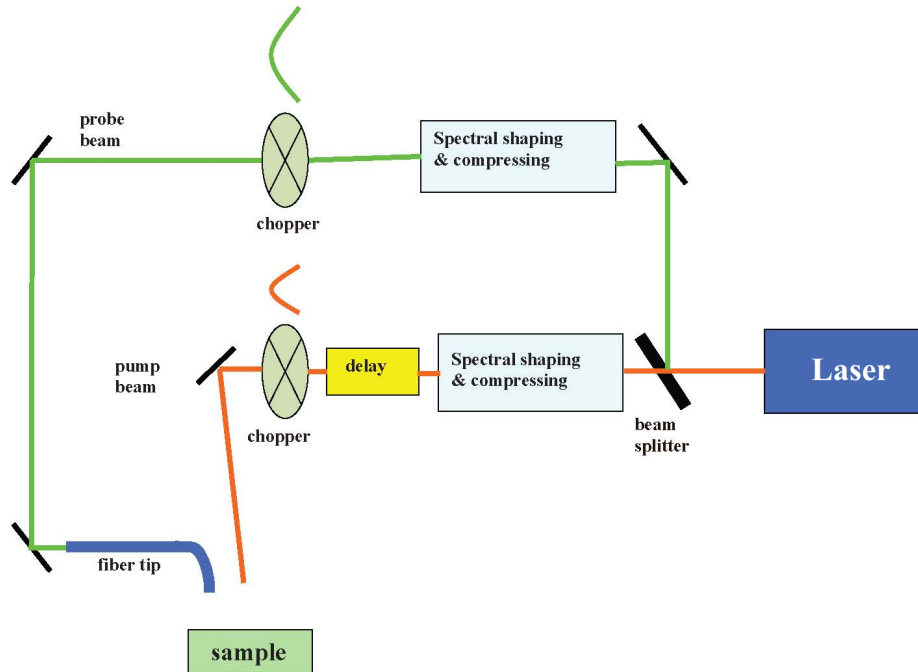
Fig. 4. The scheme of UF-SNOM setup

excitons in semiconductors and semiconducting nanostructures, since such studies require not only a high spatial resolution, but also a high resolution in time. These requirements are met by the special subtype of SNOM, UF-SNOM [14–17], which supplements SNOM by a scheme of modulation detection. Just this scheme ensures a sufficient resolution in time.

Consider its principle of action in more details (see Fig. 4). A laser pulse is divided by a splitter into two pulses. The first one, the pumping pulse, propagates to the specimen and generates carriers or excitons, and the second probing pulse is the source of a probing field for a near-field microscope which determines the distribution of generated carriers or excitons. Both beams undergo the spectral selection and the time squeezing and acquire the Gauss shape. The delay time between two pulses is determined by the duration of the delay stage in the pumping pulse tract. Thus, by varying the delay time, we can study the distribution of the concentration of carriers as static ones at different time moments, by obtaining the information about dynamical parameters of the system such as the relaxation times, coefficient of diffusion, mobility, *etc.*

In is obvious that, irrespective of the type of a microscopy, the characteristic feature of any SNOM-microscope is the direct dependence of the field intensity on a detector on a local (near) field at a point near the object where the probe is located. This means that, for the analysis of the SNOM-microscopy results, we should be able to compare the images of the intensity distribution of the field which is detected by a microscope with the near-field distribution on the object and the with the shape of the object under study. To this end, we should be able to calculate the near-field distribution on the object as a function of characteristics of the object. It is a rather nontrivial theoretical problem.

The following sections of this work are devoted just to the review of theoretical approaches which solve the posed problem. In the section "Main problem of SNOM", we will show that the problem of simulation of SNOM is reduced to the calculation of the field distribution in the system. In the section "Equation for the self-consistent field", we present the method of effective susceptibility which allows one to calculate the near-field distribution in the system. The section "Numerical simulation of SNOM images of objects with simple shape" demonstrates clearly the application of the method of effective susceptibility and presents the examples of results published by the authors earlier. In the section "Numerical simulation of images UF-SNOM", we give the application of the method of effective susceptibility to the simulation of resonance properties of systems with regard for nonlinear interactions in a
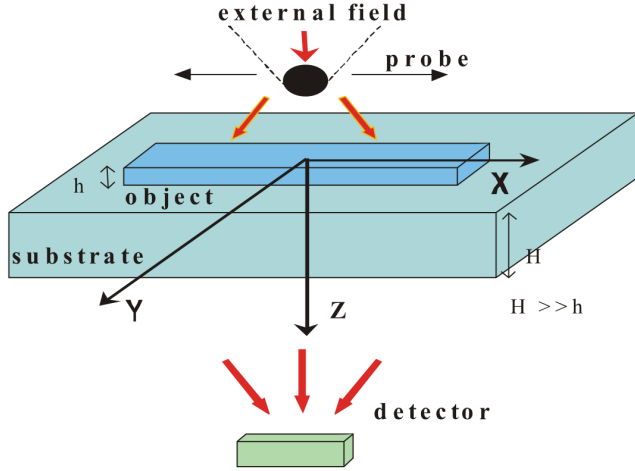
Fig. 5. The scheme of SNOM calculation

system. These new results demonstrate clearly the universality of the method of effective susceptibility in its application to the simulation of SNOM.

3. Main Problem of SNOM

Let us consider the simplified scheme of experiments of scanning near-field optical microscopy shown in Fig. 5. Though the method of calculation of a near-field on objects which is proposed in this work is universal, we will orient themselves just to this experimental scheme. In this case, it should be remembered that the sizes of an object are much less than the wavelength of a probing emission, and the distance between a detector and the system is significantly larger than these sizes. In addition, we account for that the substrate thickness is significantly larger than the linear sizes of the "object-probe" system, which allows us to neglect the influence of the lower face of the substrate on the formation of a local field on the object. These circumstances simplify essentially the calculation of a local self-consistent field on the object. For simplicity, we assume that the electric susceptibilities of the object and the probe are scalar independent of the coordinate. Then the field fixed by a detector which is positioned in the far zone is

$$\vec{E}_d(\vec{R}) = -\frac{1}{4\pi} \int\limits_{V_o} d\vec{R}' \overleftrightarrow{G}_{F-F}(\vec{R}, \vec{R}') \overleftrightarrow{\chi}(\vec{R}') \vec{E}(\vec{R}') -$$

$$-\frac{\chi_{\mathrm{P}}}{4\pi} \int\limits_{V_p} d\vec{R}' \overleftrightarrow{G}_{F-F}(\vec{R}, \vec{R}') \vec{E}(\vec{R}'). \tag{5}$$

In this formula, $\overleftrightarrow{G}_{F-F}(\vec{R}, \vec{R}')$ – Green's electrodynamic function (photon propagator) which describes the formation of the field in the far zone. The integration is performed over the volumes of an object (V_o) and a probe (V_p), i.e. over the multiply connected region. Thus, we can take a possible complicated structure of the object into account. The signal from the probe (the second term in (5) gives only a uniform illumination and depends insignificantly on the distribution of the local field on the object. In view of this, we will be interested below only in the first term in formula (5). Since the detector registers the field intensity, we will calculate the square of the modulus of a field which is scattered by the object to the point where a detector is placed. We have

$$W = \left(-\frac{1}{4\pi}\right)^2 \left| \int\limits_{V_o} d\vec{R}' G_{ik}^{F-F}(\vec{R}, \vec{R}') \chi_{kj}(\vec{R}') E_j(\vec{R}') \right|^2. \tag{6}$$

Since the distance between the object and a detector $R_d = \left| \vec{R} - \vec{R}_0 \right|$ (here, R_0 – coordinate of the center of the object) is much more than linear sizes of the object, we can consider the object to be quasipoint, by calculating intensity (6). Thus, taking the line which connects the object with a detector as the OZ axis of the Cartesian coordinate system, we can neglect the transverse components (x- and y-components) of the vector $\vec{R} - \vec{R}_0$ relative to the quantity R_d. That is, only the diagonal components of the Green tensor $\overleftrightarrow{G}_{F-F}(\vec{R}, \vec{R}')$ will considerably contribute to the intensity W:

$$W = \left(-\frac{1}{4\pi}\right)^2 \sum_i \left| G_{ii}^{F-F}(\vec{R} - \vec{R}_0) \right|^2 \times$$

$$\times \left[\int\limits_{V_o} d\vec{R}' \chi_{ij}(\vec{R}') E_j(\vec{R}') \right]^2. \tag{7}$$

The tensor parameter $C_{(L)} = \left(-\frac{1}{4\pi}\right)^2 \sum_i \left| G_{ii}^{F-F}(\vec{R} - \vec{R}_0) \right|^2$ in this formula is defined only by the properties of a measuring system (a SNOM-microscope), and its components are constant. Thus, the signal on a detector is determined by a local field in the system. So, the main problem of the theory of SNOM is to calculate the self-consistent local field at an arbitrary point of the object. We note that since the systems under consideration have

sizes which are significantly less than the wavelength of a probing emission, the local field on an object can be calculated in the near-field approximation.

4. Equation for the Self-consistent Field

The theoretical works studying the electrodynamical properties of systems within the method of local field are mainly based on the solution of the integral self-consistent Lippmann–Schwinger equation [13]

$$\vec{E}(\vec{R},\omega) = \vec{E}^{(0)}(\vec{R},\omega)-$$

$$-\frac{1}{4\pi}\int_{V_s} d\vec{R}\,'\overleftrightarrow{G}(\vec{R},\vec{R}\,',\omega)\overleftrightarrow{\chi}(\vec{R}\,',\omega)\vec{E}(\vec{R}\,',\omega). \tag{8}$$

Here, $\overleftrightarrow{G}(\vec{R},\vec{R}\,',\omega)$ – Green's function of the medium which includes the object with volume V_o. The object is characterized by the susceptibility tensor $\overleftrightarrow{\chi}(\vec{R},\omega)$ which realizes the local connection of the effective current at an arbitrary point inside the object with the full (self-consistent) field at this point

$$\vec{J}(\vec{R},\omega) = -i\omega\varepsilon_0\overleftrightarrow{\chi}(\vec{R},\omega)\vec{E}(\vec{R},\omega). \tag{9}$$

There exist several methods to solve the Lippmann–Schwinger equation (8). According to the method of discretization, the object is partitioned into small regions, in which a local field is considered steady. As a result, the integral equation (8) is replaced by the system of linear algebraic equations

$$\vec{E}(\vec{R},\omega) = \vec{E}^{(0)}(\vec{R},\omega)-$$

$$-\frac{1}{4\pi}\sum_{i=1}^{N}\overleftrightarrow{G}(\vec{R},\vec{R}_i,\omega)\overleftrightarrow{\chi}(\vec{R}_i,\omega)\vec{E}(\vec{R}_i,\omega), \tag{10}$$

which can be solved by standard algebraic methods. As usual, the number of partitions is taken quite large, so that the solutions of system (10) are determined numerically. This method is simple in applications and gives correct results under certain conditions. But its application is not correct in many cases. Indeed, only the external field slowly varies in space. As for the local field, it can be changed quite rapidly, especially on the boundaries of the object. Respectively, in order to obtain proper results, the partition along the boundaries of the object must be very fine, which leads to the significant increase in the dimensionality of system (10).

But even the fine-grained partition does not guarantee the correctness of a result. Nevertheless, the method of discretization is widely applied in SNOM [18, 19].

Another method consists in the use of the iteration procedure while solving the integral second-kind Fredholm equation [20]. The solution gives the field in the so-called Born approximation of the n-th order. The detailed analysis of such a method is presented in [21]. Despite a certain attractiveness, this method has one significant drawback: it does not allow to get the solutions corresponding to resonance interactions in the system. Indeed, let us write the Lippmann–Schwinger equation (8) in the operator form [21]

$$\vec{E} = \vec{E}^{(0)} + \overleftrightarrow{J}\vec{E}. \tag{11}$$

Here, $\overleftrightarrow{J}$ denotes the integral operator on the right-hand side of Eq. (9). The formal solution of the above equation reads

$$\vec{E} = (\overleftrightarrow{U} - \overleftrightarrow{J})^{-1}\vec{E}^{(0)}. \tag{12}$$

Here, $\overleftrightarrow{U}$ is the unit operator. It is seen that the solution which satisfies the condition $\det\left(\overleftrightarrow{U} - \overleftrightarrow{J}\right) = 0$ is resonant. On the other hand, the solution of Eq. (12) in the n-th order of the Born approximation of the iteration procedure,

$$\vec{E} = \vec{E}^{(0)} + \overleftrightarrow{J}\vec{E}^{(0)} + (\overleftrightarrow{J})^2\vec{E}^{(0)} + \ldots + (\overleftrightarrow{J})^n\vec{E}^{(0)}, \tag{13}$$

cannot have resonances. That is, any finite number of steps of the iteration procedure does not ensure a resonant solution. To get it, we need to account for the infinite number of terms of the iteration procedure. Such exact summation can be easily performed with the use of a diagram technique based on the well-approbated approach of Feynman diagrams [22,23]. The method allowing one to obtain the solutions of the self-consistent Lippmann–Schwinger equation (8) was developed in [24–29], where the analytic solution of Eq. (9) was obtained (here and below, the argument ω will be omitted) in the form

$$E_i(\vec{R}\,') = \left\{\delta_{ij} - \frac{1}{4\pi}\times\right.$$

$$\left.\times\int_{V_o} d\vec{R}\,'\Re_{ik}(\vec{R},\vec{R}\,')\mathrm{X}_{kl}(\vec{R},\vec{R}\,')e^{-i\vec{k}(\vec{R}-\vec{R}\,')}\right\}E_l^{(0)}(\vec{R}), \tag{14}$$

This formula includes the tensor of effective susceptibility of the "probe-object" system accounting for the near-field interactions in the system,

$$X_{jl}(\vec{R}\,') = \chi_{jk}(\vec{R}\,')[\delta_{lk} + S_{lk}(\vec{R}\,')]^{-1}, \tag{15}$$

where the eigen-energy part $S_{lk}(\vec{R}\,')$ is defined as the integral

$$S_{lk}(\vec{R}\,') = \int\limits_{V_s} d\vec{R}\,'' \Re_{lm}(\vec{R}\,', \vec{R}\,'')\chi_{mk}(\vec{R}\,''). \tag{16}$$

Here, we use the effective Green's function $\Re_{lm}(\vec{R}\,', \vec{R}\,'')$ which takes the rescattering of the field by the probe into account:

$$\Re_{ij}(\vec{R}, \vec{R}\,') = G_{ij}(\vec{R}, \vec{R}\,') -$$

$$- \frac{1}{4\pi} \int\limits_{V_p} d\vec{R}\,'' G_{il}(\vec{R}, \vec{R}\,'')\chi_{lk}^{(p)} G_{kj}(\vec{R}\,''', \vec{R}\,'). \tag{17}$$

The first term in (17) describes the direct propagation of the field from the point $\vec{R}\,'$ to the point $\vec{R}$. The second term describes the reemission of the field by the probe with the volume V_p and the susceptibility $\chi_{lk}^{(p)}$.

Formula (16) is written in the near-field approximation, i.e. in the case where the linear sizes of the object under study are much less than the wavelength of a scanning field. As shown in work [27], the proposed scheme allows one to go out the limits of this approximation with a modification of the formula for the eigen-energy part:

$$S_{lk}(\vec{R}\,') = \int\limits_{V_s} d\vec{R}\,'' \Re_{lm}(\vec{R}\,', \vec{R}\,'')\chi_{mk}(\vec{R}\,'')e^{-i\vec{k}(\vec{R} - \vec{R}\,')}, \tag{18}$$

That is, the application of formula (18) allows one, due to the exponential factor, to account for a change of the phase, when the light passes the distances which are comparable with the wavelength of a probing emission. In this case, we can calculate the near-field distribution on an object, whose linear sizes are much more than the wavelength of a probing emission.

As seen, solution (14) involves the case of the resonance interaction if the condition

$$\det[\delta_{lk} + S_{lk}(\vec{R}\,')] = 0 \tag{19}$$

is satisfied, and the integral in formula (14) is determined by poles of the susceptibility, which agrees

with the general principles of the theory of linear response [22].

The presented analytic method of solution was named the method of effective susceptibility. As distinct from the iteration method [20] and the method of discretization [18, 19], this method considers the resonance properties of a system and does not consume much computer time, because the numerical calculations are reduced to a simple tabulation of the formal solution onbained analytically. Two following sections will demonstrate possibilities of the method of effective susceptibility in the simulations of SNOM and UF-SNOM.

5. Numerical Simulation of SNOM Images of Objects With Simple Shape

In order to illustrate the application of the method of effective susceptibility proposed in [24–29], we calculated the near-field images for objects with various shapes which are positioned on the surface of semiconductors. The choice of objects with simple shape allowed us to perform all main calculations analytically, which confirmed additionally advantages of the proposed method.

Since SNOM gives different images for different orientations of nanostructures relative to the polarization of a probing field, we may use the mentioned method of determination of the distribution of a field in the near zone for the determination of the orientations of objects on the surface. In this case, by changing the polarization of the external field, we can get the various field distributions for the same object. Based on the results obtained, one may judge about an orientation of the object. This reasoning was taken into account on the choice of objects, for which we carried out the numerical calculations.

We considered objects with simple shape such as a parallelepiped of $120\times144\times14.4$ nm^3 in size (object P1), whose short side is oriented along the OZ axis and one of $12\times12\times120$ nm^3 in size (object P2), whose long side is oriented along the OZ axis. In addition, we considered objects in the form of a triangular pyramid, whose base is an equilateral triangle with a side of 120 nm in length and with a height of 60 nm. We assume that the the objects are made on InAs ($\varepsilon_o = 13.2$) and are placed on the GaAs substrate with ($\varepsilon_s = 13.7$). We set the wavelength of a probing emission λ600 nm. It is assumed that the probe radius is significantly less than the wavelength of a probing light and the

linear sizes of the object, namely $r_0 = 3$ nm. The dielectric susceptibility of the probe $\varepsilon_{pr} = 2.25$. With the help of numerical calculations, we find the quantity characterizing the response of the system on an external field in the near zone. With regard for the fact that the distance from a detector to the system studied on the scanning with a probe along the substrate surface is practically invariable and in view of formula (8), the field intensity on a detector can be written as

$$W = \text{const} \left| \int\limits_{V_s} d\vec{R}\,' \vec{E}(\vec{R}\,') \right|^2. \tag{20}$$

Just this quantity was calculated in the present work. We recall that $\vec{E}(\vec{R})$ is a self-consistent local field which satisfies the Lippmann–Schwinger equation (9). We present the results of the numerical analysis performed here as a map constructed on the scale of grey color. In this case, the higher field intensities correspond to lighter areas. In Fig. 6, we show the maps of the intensity distribution of the x-component of a local field in objects P1 and P2 as a function of the angle of the polarization vector of a probing light. As was mentioned above, in order to make some conclusions about the orientation and shape of the object, we have to register the field intensity with a fixed polarizationon a detector, by varying the polarization of a probing emission. In this way, we will observe the intensity distribution of the local field with fixed polarization on the object. The left column in Fig. 6 shows images of the near-field of object P1 on a change of the angle of the polarization vector ϕ from 0° to 90° relative to the OX axis: from top to bottom, $\phi = 0°, 30°, 75°, 85°, 88°$, and 90°. The distance from the scanning plane to the substrate surface $l = 30$ nm. The right column in Fig. 6 shows images of the near-field of object P2 on a change of the angle of the polarization vector ϕ from 0° to 90° relative to the OX axis: from top to bottom, $\phi = 0°, 15°, 30°, 75°, 89°$, and 90°. The distance from the scanning plane to the substrate surface $l = 240$ nm. We indicate the form of the near-field images in the case where the excitation and registration fields are normal to each other. In this case, the object rectangular in plane has the image of the near-field distribution in the form of four bright spots in regions of the vertices of the object. That is, while analyzing the objects possessing acute vertices, one needs to study the polarization dependences of a local field. Otherwise, the image of the field distribution arisen from a single object can be taken as that from several objects. Such a behavior of the image of the near-field distribution can be easily explained if we take into
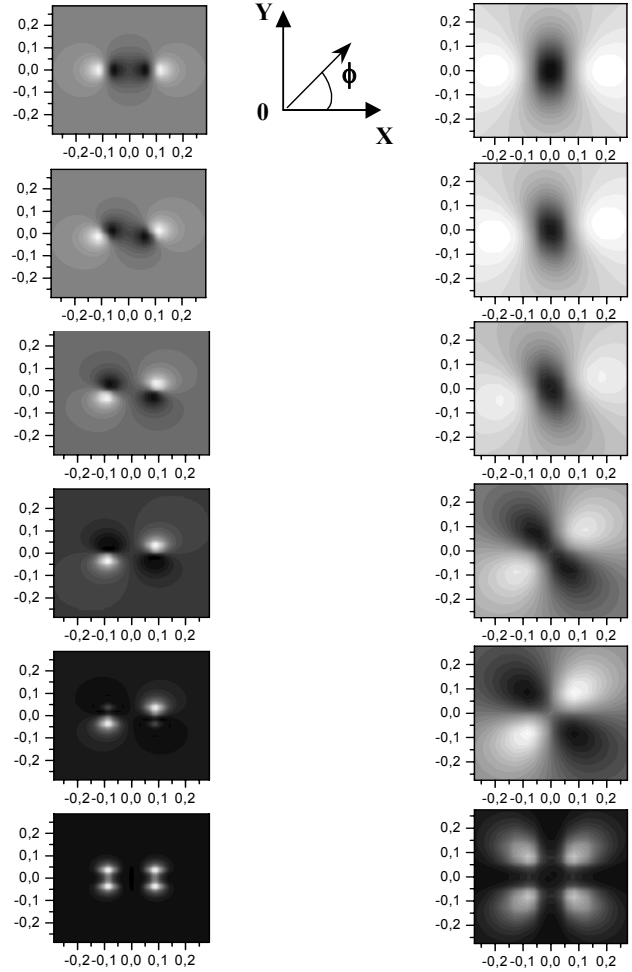
Fig. 6. Polarization properties of near-field patterns

account that the object behave itself as two dipoles parallel to its edges. It is worth noting such interesting result as the sharp transition from two maxima of the intensity to four ones, which happens in a very narrow interval of angles (88°–90°). By combining this method with polarimetry, one can attain not only a higher convenience on the determination of the orientation and form of objects, but determine some additional physical characteristics such as the coefficients of reflection, dielectric constant, *etc.*

The image of the near-field distribution for an object with a more complicated shape, a triangular pyramid, is shown in Fig. 7. Here, both the probing field and the field on a detector have the same polarization along the OX axis. The distance between the scanning plane and the substrate surface was 75 nm. This image is essentially different from the previous ones, which is caused, in
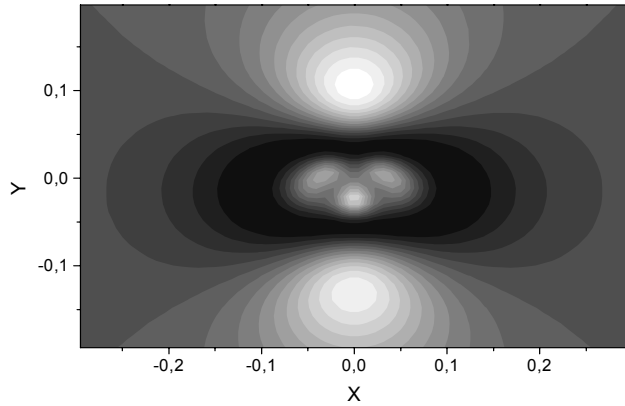
Fig. 7. Near-field pattern from a triangular pyramid made of InAS on the GaAs surface

particular, by that the local field neat the pyramid vertex has an anomalously high intensity.

Finally, we note that the method of SNOM cannot surpass the ordinary methods of tunneling or atomic force scanning microscopies in the determination of a morphology of objects or a topology of complicated surfaces. But only it allows one to visualize the distribution of evanescent fields on mesoobjects. For example, the method of SNOM efficiently registers the fields of evanescent waves in the waveguide structures on the basis of two-dimensional photon crystals, in which surface plasmon-polaritons are propagating [30]. In addition, the method of calculation of near-field images which is discussed in the present work can be successfully applied to the analysis of near-field images got within SNOM at the second-harmonic frequency. The comprehensive analysis of this approach is given in [26, 28, 29].

6. Numerical Simulation of UF-SNOM Images

Consider a Si surface (at a temperature of about 10 K) illuminated by a Gauss-like pulse of light generated by an excitonic cloud. In the course of the time, the excitonic cloud will evolve under the action of dynamical processes such as relaxation and diffusion. Therefore, by studying the distribution of excitons at some time moment after their generation, one can study the dynamical parameters of a system such, for example, as the coefficient of diffusion, relaxation duration, *etc.*

Let us consider the generation of excitons in more details. The profile of the distribution of excitons repeats the shape of the distribution of the intensity of a generating pulse and has the Gauss shape in a plane parallel to the surface. Along a normal to the surface, the distribution of excitons is determined by the Lambert–Bouguer absorption law:

$$\delta n\left(x, y, z, t=0\right) = n_m e^{-\frac{x^2}{2\sigma_{xy}^2} - \frac{y^2}{2\sigma_{xy}^2} - \frac{z}{2\sigma_z}}. \tag{21}$$

Here, $n_m = 10^{17}$ cm^{-3} (in what follows, we will give al constants with numerical values used in the calculations) is the maximum concentration of excitons, $\sigma_{xy} = 0.2\lambda$ ($\lambda = 2\pi c/\omega$) – half-width of the excitonic cloud (it is determined by the width of a generating pulse), and $\sigma_z = 0.2\lambda$ – generation degree for excitons (it is determined by the coefficient of absorption α as $\sigma_z = 1/2\alpha$).

The evolution of an excitonic cloud is described by the diffusion-drift equation for excitons [31]. This equation was solved analytically by the method of Green's functions [32]:

$$\delta n(x, y, z, t) = n_m e^{-\frac{t}{\tau}} e^{-\frac{x^2+y^2}{2\sigma_{xy}^2 + 4Dt}} \frac{\sigma_{xy}^2}{2\left(\sigma_{xy}^2 + 2Dt\right)} \times$$

$$\times \left(e^{\frac{Dt}{4\sigma_z^2} - \frac{z}{2\sigma_z}} Erfc\left[\frac{\sqrt{Dt}}{2\sigma_z} - \frac{z}{2\sigma_z}\right] + \right.$$

$$\left. + e^{\frac{Dt}{4\sigma_z^2} + \frac{z}{2\sigma_z}} Erfc\left[\frac{\sqrt{Dt}}{2\sigma_z} + \frac{z}{2\sigma_z}\right] \right), \tag{22}$$

where $D=12$ cm^2/s – the coefficient of diffusion, $\tau = 10^{-12}$ s – exciton lifetime.

Usung the calculated concentration of excitons, we can write the formula for the susceptibility of an excitonic cloud which completely represents its electrodynamical properties [33]:

$$\chi_{jl}^{(L)}(\vec{R}) = \delta_{jl}\frac{\varepsilon\omega_{LT}}{\omega_0 - \omega - i\gamma}a_B^3\delta n(x, y, z, t), \tag{23}$$

where ω is the incident light frequency (in the numerical calculations, we took $\omega = 0.99\omega_0$), $\omega_0 = 1.2$ eV – exciton resonance frequency, $\varepsilon = 11.6$ – dielectric constant of the semiconductor, $a_B = 4.5$ nm – Bohr radius, $\gamma = 0.01$ meV – homogeneous broadening caused by acoustic photons, $\omega_{LT} = 0.07$ meV – exciton longitudinal-transverse broadening.

Let the distribution of excitons be studied within UF-SNOM. Since a phase-detecting scheme of UF-SNOM allows one, due to a high resolution in time, to consider the distribution of excitons as a static one, the results of UF-SNOM experiments can be described by all
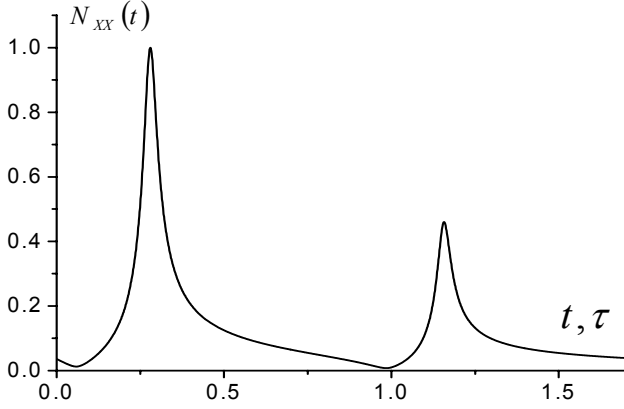
Fig. 8. Time dependence of the field intensity on a SNOM-detector

Fig. 9. Near-field image of the excitonic cloud

theoretical methods earlier developed for the simulation of SNOM. Therefore, knowing the exciton susceptibility (23), we can calculate near-field images analogously to the consideration in the previous section (by using Eqs. (23), (15), and (7).

First, let us consider the numerically obtained time dependence of the field intensity on a detector at a fixed coordinate of the probe (Fig. 8). As seen, the intensity is not a monotonous function. The presence of peaks of the intensity is related to the spatial evolution of the excitonic cloud which falls into the resonance with the field of a microscope for certain space configurations. The possibility for such resonances to exist is directly indicated, for example, by formula (15) for the effective susceptibility (the effective susceptibility has a pole). The resonances similar by their nature were earlier obtained in experiments on plasmon-polariton resonances [34].

The presence of resonance peaks (a local increase of the field) points out to the necessity to account for nonlinear interactions in the system. Therefore in the subsequent calculations, it was assumed that the susceptibility has a nonlinear third-order component

$$\chi_{jl}(\vec{R}') = \chi_{jl}^{(L)}(\vec{R}') + (\chi_{jklm}^{(N-L)}(\vec{R}')\Lambda_{km}+$$

$$+\chi_{jkml}^{(N-L)}(\vec{R}')\Lambda_{km} + \chi_{jlkm}^{(N-L)}(\vec{R}')\Lambda_{km}), \qquad (24)$$

$$\Lambda_{km} = E_k^{(}\vec{R}')\left(E_m^{(}\vec{R}')\right)^*. \qquad (25)$$

Here, $\chi_{jl}^{(L)}(\vec{R}')$ is the linear susceptibility, and $\chi_{jklm}^{(N-L)}(\vec{R}')$ is the nonlinear one. The calculation of the field on a detector with regard for nonlinear interactions

in the system requires only a slight modification of the method of effective susceptibility [26, 28, 29] considered above in details.

The results of numerical simulations of near-field images are shown in Fig. 9. The coordinates are given in the wavelength λ. The mutual position of polarizations corresponds to Fig. 6 at $\varphi = 90°$. The scanning distance is 0.2λ. The images are calculated for two time moments: $t = 0.5\tau$ (nonresonance case) and $t = 0.288\tau$ (resonance case) without regard for a nonlinearity ($\xi = 0$) and with it ($\xi = 0.0001$). Here, we introduced the notation $\xi = \chi^{(N-L)}\left(E^{(I)}\right)^2/\chi^{(L)}$. As seen, the nonlinear interactions give a minimum contribution in the nonresonance case. Therefore, they should not be considered. In the resonance case, the nonlinear interactions give a considerable contribution and strongly intensify the resonance. Therefore, their account is obligatory.

We believe that the proposed method for the calculation of the time dependence of the form of near-field images will allow one to efficiently decode the data obtained in UF-SNOM experiments and to determine such dynamical parameters of systems as, for example, the coefficient of diffusion, relaxation duration, value of a nonlinear susceptibility, *etc*.

7. Conclusions

By summarizing, we may conclude that the method of effective susceptibility is well suitable for the simulation of near-field images obtained in both ordinary scanning

near-field optical microscopy and ultrafast scanning near-field optical microscopy. This method allows one to calculate the polarization peculiarities of near-field images and the resonance properties of systems under study and to take the nonlinear interactions in the system into account. The proposed method is analytic and, therefore, does not consume many computer time for calculations. It is also quite precise. These circumstances will be useful for the efficient decoding of the data obtained in UF-SNOM experiments and the evaluation of such dynamical parameters of systems as, for example, the coefficient of diffusion, relaxation duration, value of a nonlinear susceptibility, *etc.*

1. *Lower-Dimensional Systems and Molecular Electronics*, edited by R.M. Metzger, P. Day, and G.C. Papavassilion (London: Plenum Press, 1989).

2. *Near Field Optics*, edited by D.W. Pohl and D. Courjon (Kluwer, Dordrecht, 1993).

3. A.V. Eletskii, Uspekhi Fiz. Nauk **167**, 945 (1997).

4. G. Binnig, H. Rohrer, Ch. Gerber, and E. Weigbel, Phys. Rev. Lett. **49**, 57 (1982).

5. F. Giessibl, Rev. Mod. Phys. **75**, 949 (2003).

6. D.W. Pohl, in *Advances in Optical and Electron Microscopy*, **12**, edited by C.J.R. Sheppard and T. Mulvey (Academic Press, London, 1990), p. 3734.

7. E.B. McDaniel, J.W.P. Hsu, L.S. Goldner, R.J. Tonucci, E.L. Shirley, and G.W. Bryant, Phys. Rev. B **55**, 10878 (1998).

8. V. Volkov, S. Bozhevolnyi *et al.*, Nano Letters **7**, 2341 (2007).

9. M. Born and E.W. Wolf, *Principles of Optics* (Pergamon Press, Oxford, 1991).

10. E.H. Synge, Philos. Mag. **6**, 356 (1928).

11. E.A. Ash and G. Nicholls, Nature **237**, 510 (1972).

12. W. Pohl, W. Denk, and M. Lanz, Appl. Phys. Lett. **44**, 651 (1984).

13. J.-J. Greffet and R. Carminati, Prog. Surf. Sci. **56**, 133 (1997).

14. V. Emiliani, T. Guenther, C. Lienau *et al.*, J. of Microscopy **202**, 229 (2001).

15. A. Richter, G. Behme, M. Süptitz, Ch. Lienau *et al.*, Phys. Rev. Lett. **79**, 2145 (1997).

16. V. Emiliani, T. Guenther, and Ch. Lienau, Phys. Rev. B **61**, R10583 (2000).

17. A. Richter, M. Süptitz, Ch. Lienau *et al.*, J. of Microscopy **194**, 393 (1999).

18. L. Novotny, JOSA A **14**, 91 (1997).

19. M. Xiao and S. Bozhevolnyi, Opt. Commun. **130**, 337 (1996).

20. P.M. Morse and H. Feshbach, *Methods of Theoretical Physics* (McGraw-Hill, New York, 1953).

21. O. Keller, M. Xiao, and S. Bozhevolnyi, Surf. Sci. **280**, 217 (1993).

22. A.A. Abrikosov, L.P. Gorkov, and I.E. Dzyaloshinsky, *Methods of Quantum Field Theory in Statistical Physics* (Dover, New York, 1975)..

23. R.D. Mattuck, *A Guide to Feynman Diagrams in the Many-Body Problems* (McGraw-Hill, New York, 1967).

24. S. Bozhevolnyi and V. Lozovski, SPQEO **2**, 45 (1999).

25. S. Bozhevolnyi and V. Lozovski, Phys. Rev. B **61**, 11139 (2000).

26. V. Lozovski, Yu. Nazarok, and S. Bozhevolnyi, Physica E **11**, 323 (2001).

27. S. Bozhevolnyi and V. Lozovski, Physica E **15,** 229 (2002).

28. S. Bozhevolnyi and V. Lozovski, Phys. Rev. B **65**, 235420 (2002).

29. G.-R. Yang, X.F. Ma, W.X. Chen *et al.*, Appl. Phys. Lett. **64**, 533 (1994).

30. S. Bozhevolnyi, V. Volkov, and K. Leosson, Phys. Rev. Lett. **89**, 186801 (2002).

31. M.A. Tamor and J.P. Wolfe, Phys. Rev. Lett. **44**, 1703 (1980).

32. A.D. Polyanin, *Handbook of Linear Partial Differential Equations for Engineers and Scientists* (Chapman and Hall/CRC Press, Boca Raton, 2002).

33. A. Kavokin and G. Malpuech, *Cavity Polaritons* (Elsevier, Amsterdam, 2003).

34. V. Chegel, Yu. Shirshov *et al.*, J. of Bioch. Biophys. Meth. **50**, 201 (2002).

ЗАСТОСУВАННЯ МЕТОДУ ЕФЕКТИВНОЇ СПРИЙНЯТЛИВОСТІ ДО МОДЕЛЮВАННЯ СКАНУЮЧОЇ ОПТИЧНОЇ МІКРОСКОПІЇ БЛИЖНЬОГО ПОЛЯ

В.О. Василенко, В.З. Лозовський

Р е з ю м е

Розглянуто особливості формування картин ближнього поля як в звичайній скануючій оптичній мікроскопії ближнього поля, так і в надшвидкій скануючій оптичній мікроскопії ближнього поля. Обговорено метод ефективної сприйнятливості для обчислення картин ближнього поля. Метод ґрунтується на аналітичному розв'язку рівняння Ліппмана–Швінгера. На прикладах об'єктів простої форми – паралелепіпеда та трикутної піраміди продемонстровано результати чисельних розрахунків картин ближнього поля. Показана залежність вигляду ближньопольової картини від взаємної орієнтації векторів поляризації зондуючого поля мікроскопа і поля, що реєструється детектором. Наведено результати чисельних розрахунків картин ближнього поля, які отримують в надшвидкій скануючій оптичній мікроскопії ближнього поля під час дослідження екситонної хмари, згенерованої імпульсом лазера. Проведено чисельний аналіз просторових конфігураційних резонансів екситонної хмари яка релаксує. Показано, що у цьому випадку необхідно враховувати нелінійні взаємодії в системі.